Materials Today • Volume xxx, Number xx • xxxx 2025

Unveiling the contact electrification of triboelectric fibers by exploring their unique micro- and macroscale structural properties

Renwei Cheng [a,b,c,1], Chuanhui Wei [a,b,1], Chuan Ning [a,b], Tianmei Lv [a,b], Xiao Peng [d], Zhong Lin Wang [a,b,e,f], Kai Dong [a,b,*]

[a] CAS Center for Excellence in Nanoscience, Beijing Key Laboratory of Micro-Nano Energy and Sensor, Beijing Institute of Nanoenergy and Nanosystems, Chinese Academy of Sciences, Beijing 101400 China
[b] School of Nanoscience and Engineering, University of Chinese Academy of Sciences, Beijing 100049 China
[c] Department of Materials Science and Engineering, Southern University of Science and Technology, Shenzhen, 518055, China
[d] Key Laboratory of Organic Optoelectronics and Molecular Engineering of the Ministry of Education, Department of Chemistry, Tsinghua University, Beijing 100084, PR China
[e] School of Material Science and Engineering, Georgia Institute of Technology, Atlanta, GA 30332, United States
[f] Yonsei Frontier Lab, Yonsei University, Seoul 03722, Republic of Korea

The emerging triboelectric fibers or textiles have recently attracted widespread attention due to their unique wearable energy supply and self-powered sensing functions. However, the unique micro- and macrostructural effects of triboelectric fibers on contact-electrificaion (CE) have not been systematically studied, which result in the lower charge output compared to conventional film structure. Here, in order to provide theoretical guidance for designing high-performance triboelectric fibers with optimized structural designs, a systematic experimental measurement and theoretical analysis method is developed to explore the influence laws and potential mechanisms of the surface microstructural defects and overall macrostructural compositions of triboelectric fibers on their CE behaviors. It can be found that the surface microstructure defects contribute to increasing the total charge transfer, due to the increase in effective interface contact area. In addition, triboelectric fibers with core–shell coaxial structure prepared by uniform coating method have higher electrical output performance, which can ensure maximum contact between the conductive layer and the dielectric layer. This work provides a new research paradigm for studying the CE behavior and quantifying surface charges of complex structures, and suggests a multiscale structural design strategy for high-performance triboelectric fibers.

Keywords: Triboelectric fibers; Contact-electrification; Surface charge distribution; Microstructural defects; Macrostructural compositions

Introduction

Contact-electrification (CE)/triboelectrification of polymer dielectrics is a universal but extremely complex phenomenon [1–3], but its evolution laws and underlying mechanisms have always troubled us [4–6]. Recently, inspired by the mechano-electric conversion effect, the newly developed triboelectric nanogenerators have shown great application prospects in mechanical energy harvesting [7–10], flexible passive sensors [11–13], and other fields [14–16]. It is well known that the CE behavior is influenced or constrained by many factors, including environmental conditions [17,18], structural characteristics [19,20], material intrinsic properties [21,22], etc. Among them, structural construction is a crucial characteristic parameter that

* Corresponding author at: CAS Center for Excellence in Nanoscience, Beijing Key Laboratory of Micro-Nano Energy and Sensor, Beijing Institute of Nanoenergy and Nanosystems, Chinese Academy of Sciences, Beijing 101400, China.
E-mail address: Dong, K. (dongkai@binn.cas.cn)

[1] R. Cheng and C. Wei contributed equally to this work.

 https://doi.org/10.1016/j.mattod.2025.01.013

Please cite this article in press as: R. Cheng et al., Materials Today (2025), https://doi.org/10.1016/j.mattod.2025.01.013

directly determines the relative working mode and effective contact area, which is closely related to the total interface transferred charge [23,24].

Polymer fibers exhibit high aspect ratio, large curvature, high softness, and high freedom of movement, which are an idea attachment carrier for wearable electronics [25]. By integrating the mechano-electric conversion technology with traditional textile processes, a new kind of smart textiles named as triboelectric fibers or textiles have been endowed with autonomous power supplying and self-powered sensing functions while retaining the original wearing comfort, which can achieve human energy and sensing needs in a self-sufficiency mode [26]. The unique structural characteristics of the fibers allow them to achieve a new power mode such as volumetric electromechanical response [27,28]. The surface microstructural defects and overall macrostructural composition of triboelectric fibers will seriously affect their CE behaviors [29]. The surface of polymer fibers is not smooth and exists numerous irregular micro/nanoscale defects, such as convex, concave, crack and hairiness [30,31]. The surface defects can alter the magnitude and distribution of the mechanically induced local electric field. In addition, the macrostructural composition of triboelectric fibers is composed of at least a conductive layer and a dielectric layer. The encapsulation method of the dielectric layer and the arrangement of the two also greatly affect the whole electrical output performance [32,33]. Unfortunately, the impact laws and potential mechanisms of microscopic and macroscopic structural effects on CE are still ambiguous, making it difficult to achieve quantitative design of high-performance triboelectric fibers from a structural perspective.

The high-precision quantitative measurement of surface charge density and its geometric distribution is a fundamental method for in-depth exploring the macro-to microscale structural effect of triboelectric fibers on CE behaviors [34,35]. The standardized test method for obtaining charge density through cyclic contact-separation motion under controllable environmental conditions is widely used to determine the triboelectric series of different film-like structural materials [36,37]. However, the accuracy of this test method largely depends on sufficient contact between the interfaces, almost ignoring the structural effects. In addition to direct measurement of charge density, Kelvin probe force microscope (KPFM) and electrostatic voltmeter are also widely utilized to measure and visualize the nanoscopic and macroscopic surface potential distribution, respectively [38–40]. KPFM can only sweep range below $10 \times 10\ \mu m^2$ and has high requirements for the roughness of the sample surface, and the testing difficulty is relatively high. Although electrostatic voltmeters can quickly and conveniently detect macroscopic potential distribution, its accuracy is limited by the size of the probe, making it difficult to accurately measure microscopic potential distribution. Therefore, new strategy is required for exploring the CE behaviors of triboelectric devices with special structures, such as polymer dielectric fibers.

In this paper, by combining quantitative experimental measurements and finite element analysis methods, the influence laws and potential mechanisms of surface microstructural defects and overall macrostructural composition of triboelectric fiber on its CE behaviors are systematically explored. Four types of surface microstructures are controllably constructed through molding methods, including convex, concave, crack and hairiness. In addition, two encapsulation modes of surface dielectric layers including spiral coiling or uniform coating, and two combination modes between conductive layers and dielectric layers including parallel and coaxial arrangement are designed. It can be found that the microstructural defects on the surface of triboelectric fibers contribute to increasing the amount of charge transfer, due to the charge enrichment induced by local stress concentration. The accumulation of charges caused by the curved surfaces of fibers is more likely to lead to charge dissipation. Compared to spiral coiling, the uniform coating mode can achieve uniform stress distribution and larger effective contact area, thus resulting in more homogeneous and more charge distribution. Moreover, coaxial combination is more advantageous than parallel arrangement in increasing the effective contact area between the inner electrode layer and the outer dielectric layer, especially for low modulus dielectric materials. In summary, the CE behaviors of triboelectric fibers are investigated from multi-scale structure perspectives, which shows important guiding significance for studying the charge transfer mechanism of devices with complex structural characteristics.

Results

Microstructure and macrostructure effects of triboelectric fibers

Structural feature is one of the most crucial factors influencing CE behaviors. Different from film structure, fibers with high length-diameter ratios, curved contour, soft texture, and uneven surface morphology exhibit distinctive macrostructure and microstructure effects. In order to quantitatively analyze the effect of microstructural defects on the CE, four kinds of surface microstructural defects, including convex, concave, crack, and hairiness, are delicately constructed on the surface of dielectric fibers through 3D printing method (Fig. 1a). For the convenience of study, the complex three-dimensional geometric structures of microstructural defects are simplified into two-dimensional cross-sectional structures, as shown in the left side of Fig. 1b. The surface charge distributions of different microstructural defects in contact state are illustrated in the right side of Fig. 1b, from which the charge enrichment region can be observed. In addition, the macrostructure of triboelectric fibers mainly involves the encapsulation method of the surface dielectric layer and the combination method of the conductive layer and the dielectric layer (Fig. 1c and d). According to the preparation process of the dielectric layer, there are mainly two common encapsulation methods, such as uniform coating and spiral coiling (Fig. 1c). Based on the relative position of the conductive layer and dielectric layer, typical combinations of triboelectric fibers include parallel arrangement and coaxial arrangement (Fig. 1d) [23]. The surface charge distribution of different combinations of macrostructures is shown in Fig. 1e and f, which clearly indicate the differences in CE behaviors caused by structure effects.

In order to explore the CE process of triboelectric fibers, it is necessary to quantitatively investigate the dynamic changes of charge transfer between conductive fibers and dielectric fibers during progressive loading. As the distance between conductive

Please cite this article in press as: R. Cheng et al., Materials Today (2025), https://doi.org/10.1016/j.mattod.2025.01.013

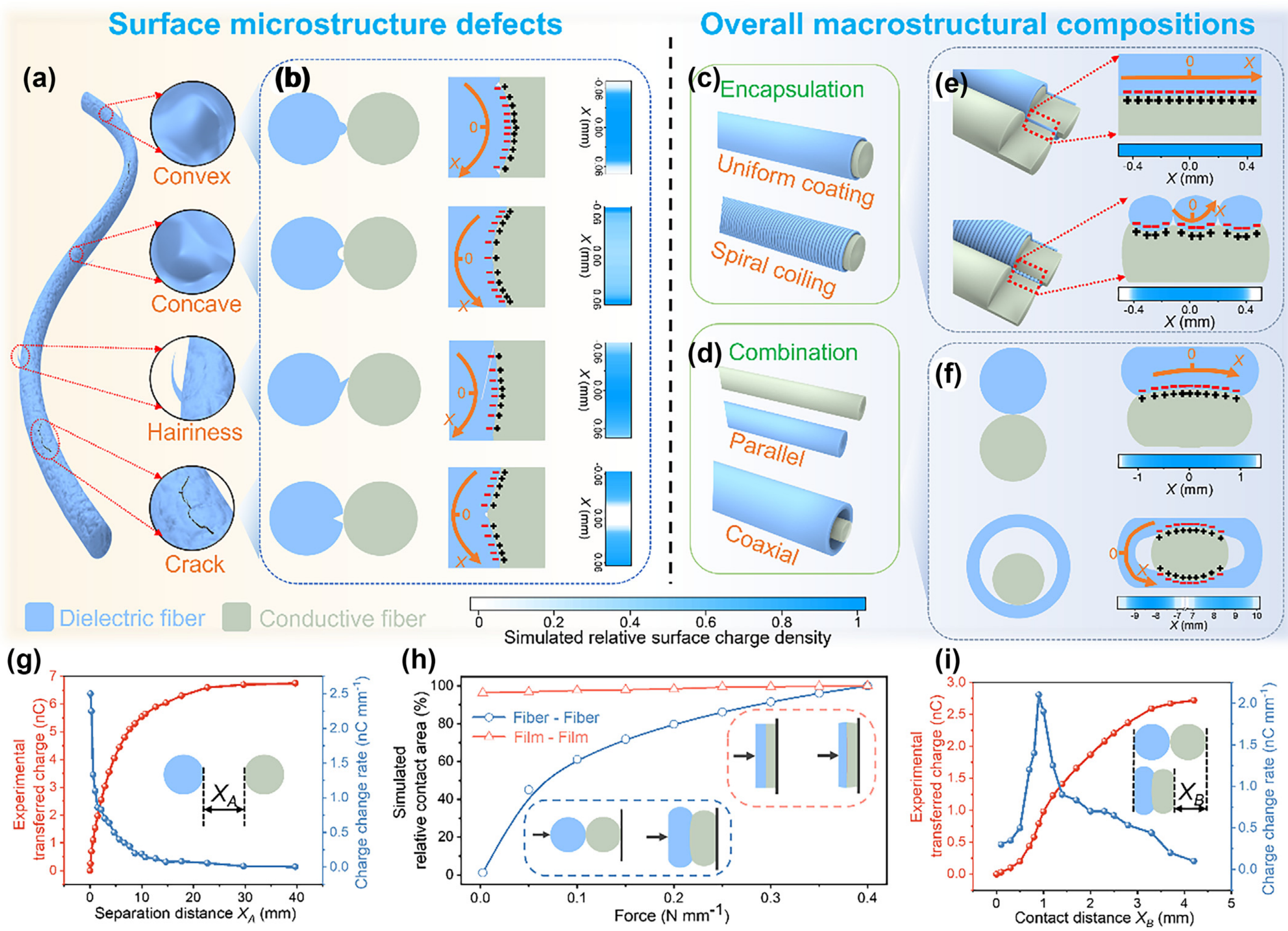

FIG. 1

Microstructure and macrostructure effects of triboelectric fibers. (a) Schematic diagrams of the triboelectric fibers with various surface microstructural defects on the surface of dielectric layer. (b) Two-dimensional cross-sectional view (left), schematic diagram of surface charge distributions at the contact interface (middle), and simulated relative charge density distributions (right) of the triboelectric fibers with the four surface microstructural defects. (c–d) Overall macrostructural compositions of the triboelectric fiber including different encapsulation methods of dielectric layer (c) and different combination methods between dielectric layer and conductive layer (d). (e–f) Cross-sectional view (left), surface charge distribution (top right), and simulated relative charge density distributions (bottom right) of different encapsulation (e) and combination (f) methods. (g) Experimental transferred charges and charge change rates of the fiber–fiber under different separation distances of X_A. (h) Compare the variation trend of relative effective contact area between the fiber–fiber and the film-film under progressive loading. The insets are the cross-sectional view of the fiber–fiber and the film-film. (i) Experimental transferred charges and charge change rates of the fiber–fiber under different contact distances of X_B.

fibers and dielectric fibers continues to decrease, their relative state undergoes a transition from gradually decreasing separation distance to just coming into contact and then increasing contact area (Fig. S1a). When conductive fibers and dielectric fibers are in a non-contact state, the transferred charge increases with the increase of the non-contact displacement (X_A) and tends to saturate at the X_A of approximately 30 mm, due to the effect of electrostatic induction (Fig. 1g). The saturation of transferred charges in non-contact state indicates the existence of an optimal distance between the conductive layer and the dielectric layer. In addition, charge change rate gradually decreases with increasing distance, indicating that the closer the distance between the two, the stronger the electrostatic induction effect. When the two reach initial contact, the trend of effective contact area change between the fiber–fiber and the film-film with increasing progressive loads is analyzed and compared. As shown in Fig. 1h, the effective contact area of the film-film contact with a flat surface hardly changes with increasing load, indicating that the effective contact area of film structure almost reaches saturation once contact. However, as the load increases, the contact interface of the fiber–fiber with curved surfaces changes from linear contact to surface contact, and the contact area continues to increase until saturation. As shown in Fig. 1i, the transferred charge gradually increases with the increasing of the post-contact displacement (X_B), due to the coupling effect of CE and electrostatic induction. Furthermore, with the increasing of the X_B, the rate of charge change undergoes a trend of first increasing and then decreasing. The maximum variation rate can be obtained when the X_B is 0.9 mm. Therefore, there is also an optimal contact distance with maximum charge growth rate. The comparison of the relative charge transfer between the fiber–fiber and the film-film in the separation and contact states is also discussed in Fig. S1b, which

Please cite this article in press as: R. Cheng et al., Materials Today (2025), https://doi.org/10.1016/j.mattod.2025.01.013

is consistent with the trend of effective contact area change, indicating that the structural differences between fibers and films lead to different CE behaviors.

Novel microscale surface charge density distribution characterization method

Accurate quantitative measurement of surface charge density and its distribution is a fundamental strategy for exploring the change rules and potential mechanisms of CE behaviors in triboelectric fibers. KPFM and electrostatic voltmeter are commonly used to measure and visualize surface potential or charge distribution. However, due to the limitations of the size and movement distance of scanning probes, KPFM is suitable for nanoscale applications, while electrostatic voltmeters are more inclined to measure the millimeter or centimeter scale. Therefore, there is still a lack of an effective characterization method that can accurately measure charge density distribution at the micrometer scale. In previous studies, it has been found that the transferred charge is highly correlated with the contact stress at the interface [41,42], and charge density increases with increasing interfacial stress [43–45]. Therefore, by establishing a functional correlation between stress state and charge state, it may be possible to calculate the distribution of surface charge density through stress distribution. The flowchart of the method for calculating charge density is displayed in Fig. 2a. Firstly, the material parameters can be obtained by fitting the stress–strain curve with the Mooney-Rivlin model and then substituted into the simulation software to calculate the stress distribution. Secondly, by fitting the experimental data with quartile polynomial, the functional relationship between stress and charge density can be gained. Ultimately, the charge density distribution can be calculated by combining the simulated stress distribution and experimental function relationship between stress and charge density.

In this work, dielectric fibers prepared from ecoflex and conductive fibers filled with carbon micro/nanofibers in ecoflex are selected to study the CE behaviors of triboelectric fibers due to their excellent structural malleability. The functional group of the dielectric fiber is revealed by the ATR-FTIR spectra (Fig. S2). The stress–strain curves of the dielectric fiber and the conductive fiber are well fitted with the Mooney-Rivlin model (Fig. S3). Subsequently, the relationship between stress and charge density can be well fitted. As shown in Fig. 2b, as the stress increases, the surface potential will gradually increase until saturation is reached. The schematic diagram of contact-separation measurement is shown in Fig. S4. After sufficient contact with the conductive film, the average potentials of the dielectric film under different loadings are obtained through an electrostatic voltmeter (Fig. 2c). The loading frequency is 2 Hz, stress varies from 1.45 kPa to 101.53 kPa. It can be found that the evolution trend of surface potential under different stresses is consistent with the change trend of charge density in Fig. 2b, further verifying the accuracy of the established function correlation between stress and charge density (Table S1). Moreover, the surface charge density distribution predicated using the stress-charge functional relations (Fig. 2d) shows good consistency with the experimental surface potential distribution (Fig. 2e). The percentage of the experimental and simulated values is close, verifying the accuracy of the novel microscale surface charge density distribution characterization method (Table S2). Therefore, based on this functional relationship between stress and charge density, the local micrometer scale charge density distribution on the surface of dielectric fibers can be calculated in subsequent analysis.

It is based on this functional relationship that the simulation results of transferred charges are derived by measuring the stress variation of the dielectric fiber during dynamic loading, and further compared with the experimentally measured transferred charges. As shown in Fig. 2f, the simulated charges of dielectric fibers are in good agreement with the experimental results. The cross-sectional charge density distributions of the dielectric fiber under different stresses are calculated (Fig. 2g). The cross-sectional coordinate distribution of dielectric fibers is shown in the inset of Fig. 2g. It can be observed that both the contact area and charge density increase with the increase of external force. Moreover, there exists charge density saturation platforms that extend along the fiber contact point to both sides, especially under high stress conditions. By fixing the probe and rotating the dielectric fiber to measure its surface potential distribution (the inset in Fig. 2h), the reliability of the derived charge density distribution can be further verified (Fig. 2h). In addition, several dielectric fibers with variable radius R_0 are also investigated under the fixed force of 0.3 N mm^{-1}, which further verifies the accuracy of the developed charge density characterization method (Fig. S5a and b). The surface charge density measurement strategy proposed in our work based on the correlation between stress and charge is not only applicable to complex geometric structures, but also suitable for a wide range of scales, providing a new methodology for exploring the mechanism of CE. The comparison of this strategy with two other commonly used methods including KPFM and electrostatic voltmeter is summarized in Table S3 and further discussed in Note S1.

Comparison of CE behaviors between fiber structure and film structure

Compared with the CE behaviors of the plane film structure which has been well studied [5,46], the CE behaviors of the curved fiber structures are rarely explored. In order to accurately grasp the influence law and potential mechanism of fiber structure on CE, the differences in CE behavior between fibers and films are firstly investigated. Three types of contact pairs have been selected, including fiber–fiber, fiber-film, and film-film (Fig. 3a). Frequency is one of the most common influencing factors in CE, which is generally considered to not affect the transferred charge under ideal situations [47,48]. However, the transferred charge can be varied by multiple factors in practical conditions [49–51]. The transferred charge of the fiber–fiber type is measured under varied frequencies, which shows a trend of first increasing and then gradually saturating (Fig. S6). The transferred charge of the fiber–fiber is reduced by 67 % when the frequency decreases from 2.5 Hz to 0.05 Hz, indicating a more severe degree of charge dissipation at low frequencies. The contact time of the charged dielectric fiber with air and conductor increases at low frequencies, which exacerbates charge dissipation. Therefore, the transferred charge decreases with decreasing frequency. The relative charge changes of fiber–fiber, fiber-film and film-film at high (2.5 Hz) and low (0.05 Hz) frequencies is

Please cite this article in press as: R. Cheng et al., Materials Today (2025), https://doi.org/10.1016/j.mattod.2025.01.013

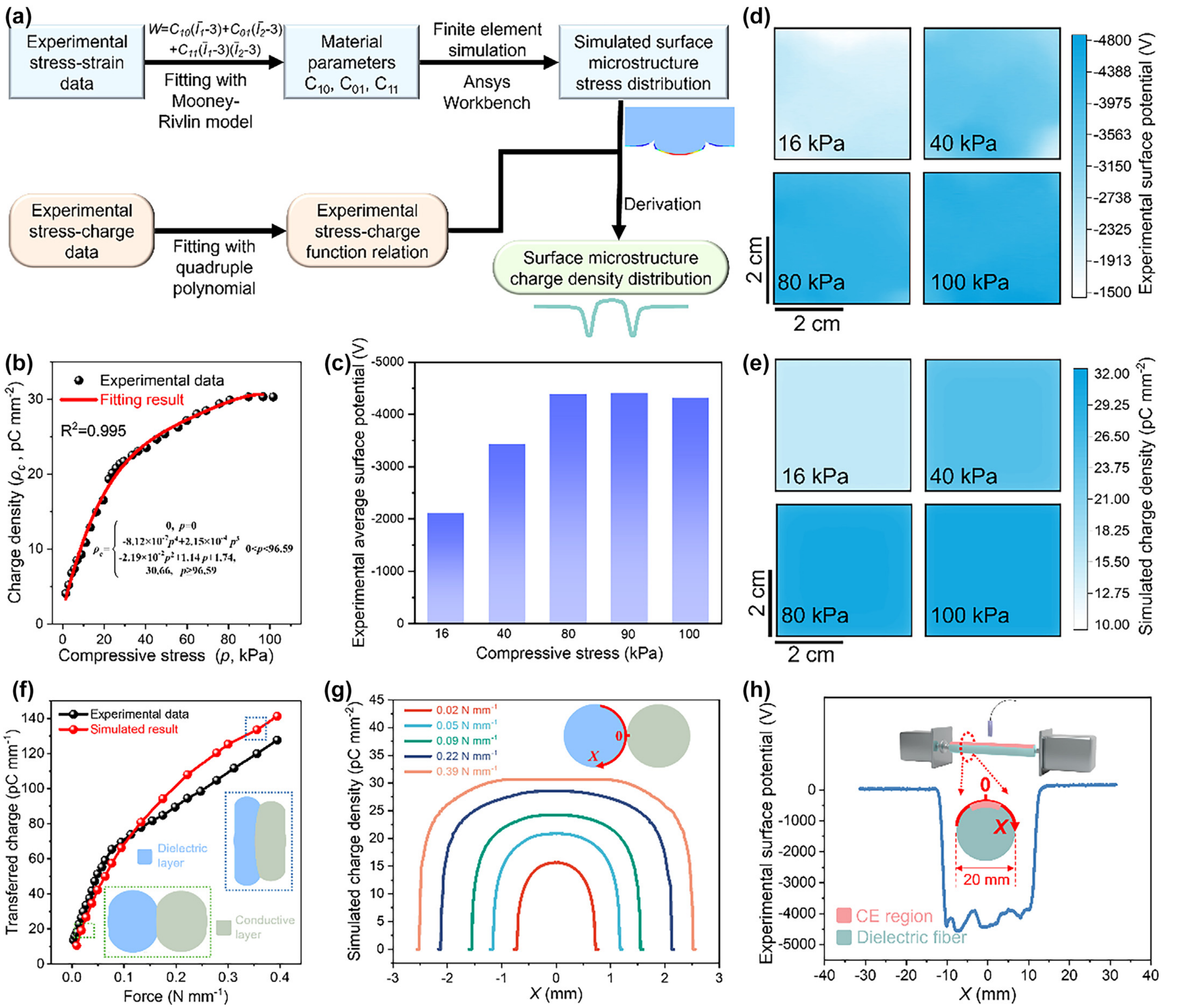

FIG. 2

Novel microscale surface charge density distribution characterization method. (a) Flowchart of establishing the function correlation between surface stress distribution and surface charge density distribution. (b) The function curve of surface charge density and compressive stress measured experimentally. (c) Experimental average surface potential of the dielectric film under different compression stresses. (d and e) Experimental surface potential distribution (d) and simulated charge density distribution (e) of the dielectric film under different compression stresses, including 16, 40, 80, and 100 kPa. (f) Comparison of experimental and simulated transferred charges under progressive loading. The insets show the variation in the contact state between conductive fibers and dielectric fibers. (g) Simulated charge density distributions at the cross-section of the contact interface under different loadings. The inset is the diagram of the coordinate system. (h) Radial surface potential distribution of the large-diameter fiber (20 mm). The inset is the schematic diagram of the method for measuring the surface potential of the large-diameter fiber.

shown in Fig. 3b, indicating that the charge dissipation of the fiber-film is largest. To explain the underlying reasons, the distribution of stress and charge density is obtained from simulation calculation. As shown in Fig. 3c and d, the stress and charge density of the fiber-film are the highest within a large length range. The corresponding stress nephograms are shown in Fig. S7. The surface potentials of the three contact types are measured and compared in Fig. 3e, verifying the simulated results in Fig. 3d. In addition, with the increase of external forces, more significant charge dissipation occurs (Fig. S8). Furthermore, a larger film thickness or fiber diameter will reduce the stress and charge density distribution of the fiber-film, due to lower deformation tolerance (Fig. S9 and Note S2).

It is well known that the accumulated charge of polymer dielectrics is more easily dissipated by the conductor in contact state, while in non-contact state, they can only be dissipated by moisture or heat [52–54]. For this purpose, the relative charge residuals of the three contact types are investigated at different interval times, including uninterrupted, maintaining separation for 5 s, and maintaining contact for 5 s. As shown in Fig. 3f,

Please cite this article in press as: R. Cheng et al., Materials Today (2025), https://doi.org/10.1016/j.mattod.2025.01.013

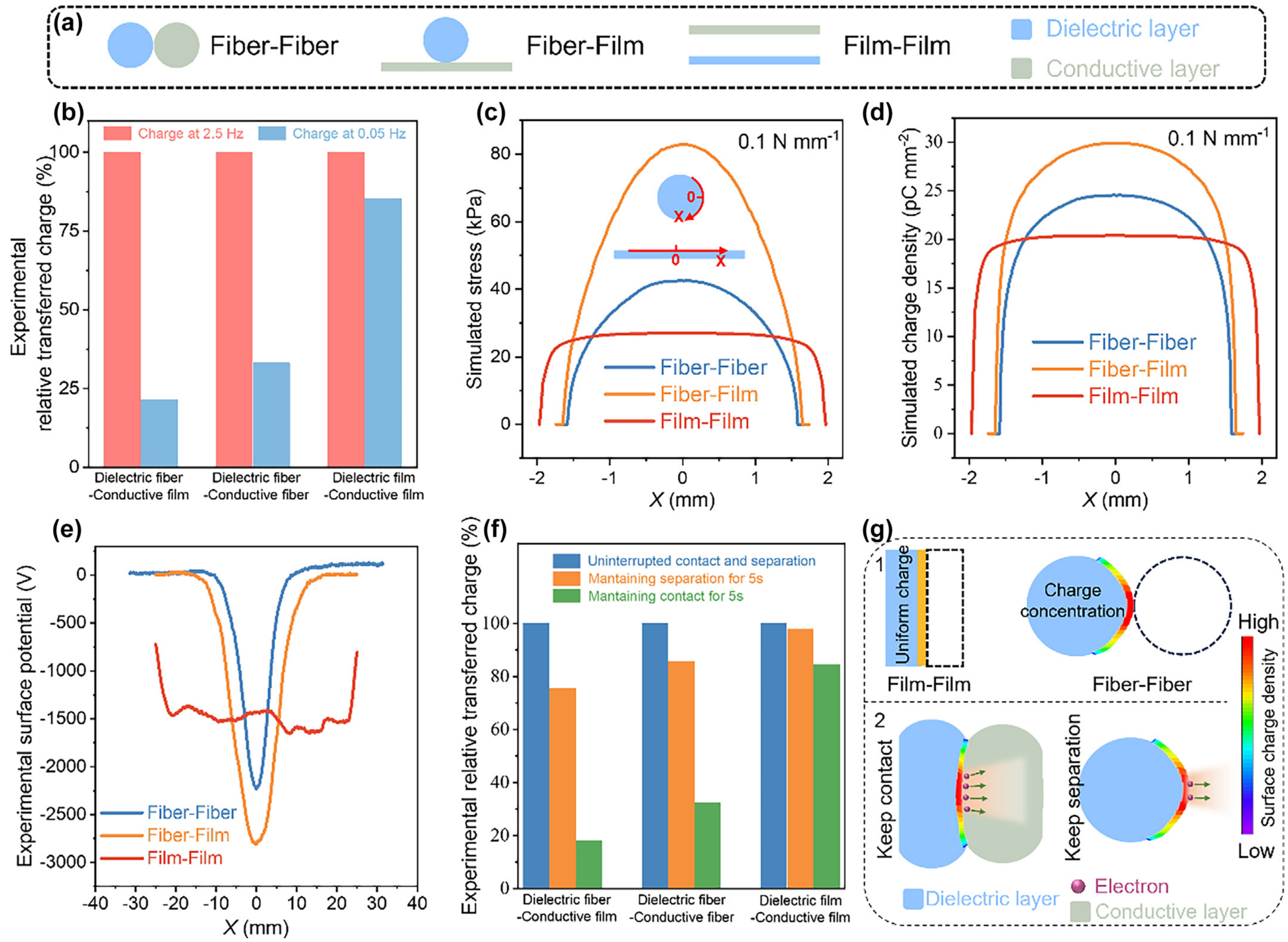

FIG. 3

Comparison of the CE behaviors between fiber structure and film structure. (a) Cross-sectional schematic diagrams of different contact pairs, including the fiber–fiber, the fiber-film, and the film-film. (b) Comparison of experimental relative transferred charges among the three contact pairs under high (2.5 Hz) and low (0.05 Hz) frequencies. (c and d) Simulated cross-sectional stress (c) and charge density distributions (d) of the dielectric layers in the fiber–fiber, fiber-film, and film-film. (e) Experimental surface potential distributions of the dielectric layers in the fiber–fiber, fiber-film, and film-film. (f) Comparison of experimental relative transferred charges among the three contact pairs of fiber–fiber, fiber-film, and film-film under different motion states, such as uninterrupted contact-separation state, maintaining separation state for 5 s, and maintaining contact state for 5 s. (g) Schematic diagrams of the surface charge distribution between film-film and fiber–fiber (g1) and the charge dissipation pathways between maintaining contact state and maintaining separation state (g2).

the contact state is more likely to cause charge dissipation compared to the separated state, because conductors in contact state are more prone to charge loss compared to air. The charge decay trends within 5 s for continuous contact or continuous separation state are shown in Fig. S10 and discussed in Note S3. In addition, as the number of cycles increases, the amount of transferred charge and the charge decay rate gradually decrease until they stabilize, and the decay rate is faster in the continuous contact state (Fig. S11). The potential charge dissipation mechanism under different structures or working states has also been further explored. As shown in Fig. 3g, due to the stress concentration of curved fibers at the contact position, the charge accumulation area has a higher charge dissipation ability compared to film structures with uniformly distributed charges. Additionally, due to the strong charge transport capability of conductors, the amount of charge dissipation in the contact state is greater. This article further analyzes the differences in CE among the three contact types from a simulation perspective. It can be found that the fiber-film type has a larger effective contact area, resulting in the highest amount of charge transfer (Fig. S12). The CE behaviors between dielectric fibers and conductive fibers are further studied in terms of contact angle, axial staggered distance, and contact length. It is found that the larger the contact angle, the smaller the contact area, and the less charge is transferred (Fig. S13). And the larger the axial staggered distance, the smaller the effective contact area and the less transferred charge (Fig. S14). Moreover, the transferred charge almost linearly increases with the length owing to the uniformity of potential distribution in the axial direction (Fig. S15).

Influence of surface microstructure defects on CE

Although several studies have attempted to improve the electrical output or sensing response capability of triboelectric devices through microstructure design (Table S4 and Note S4), the influ-

Please cite this article in press as: R. Cheng et al., Materials Today (2025), https://doi.org/10.1016/j.mattod.2025.01.013

ence laws and potential mechanisms of surface microstructures on CE behaviors have not been discussed in detail due to the lack of quantitative analysis methods. As the SEM images shown in Fig. S16, there are numerous microscale structural defects on the surface of triboelectric fibers, mainly including convex, concave, hairiness and crack. The four microstructures are selected and further simplified into two-dimensional models for easy analysis. The precise and controllable construction of different microstructural defects is achieved through 3D printing method (Fig. S17). The detailed modeling method of the four microstructural defects is discussed in Note S5. The relative increase of charges in local areas with and without defects is simulated and calculated based on the function correlation relationship between stress and charge to explore the effect of defect types on local charge distribution. The calculation method for the relative increase in charge is explained in Fig. S18 and Note S6. The simulated results indicate that the relative charge increments of the four defects all increase with the increase of force (Fig. 4a), which can be attributed to the gradual increase in effective contact area and average stress of the defects (Fig. S19a and S19b). The measured transferred charges of dielectric fibers with different defects after contact with conductive fibers are shown in Fig. S17b, from which the charge increments can be further obtained (Fig. 4b). It can be found that the charge increment

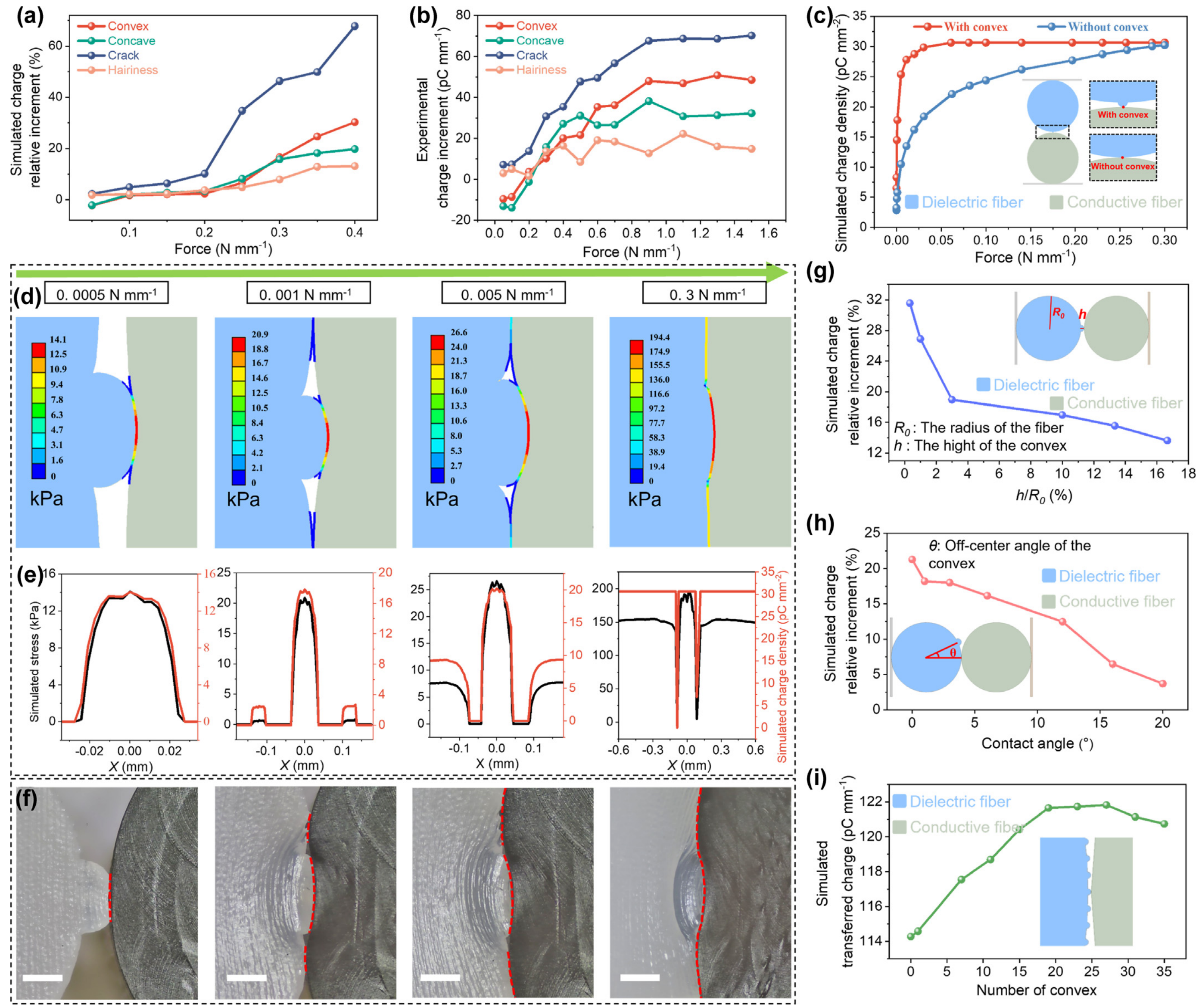

FIG. 4

Influence of surface microstructural defects on CE behaviors. (a and b) The simulated charge relative increment (a) and experimental charge increment (b) of the triboelectric fibers with different surface microstructural defects in the dielectric layer. (c) Comparison of simulated charge density of triboelectric fibers with and without convex defect at the contact center. The inset is a schematic cross-sectional view of the contact center with and without convex defect. (d–f) Simulated stress distribution nephogram (d), simulated cross-sectional stress and charge density distribution (e), and physical photograhs (f) of the dielectric fiber with convex defect. Scale bar is 3 mm. (g and h) Simulated charge relative increments of dielectric fibers with different ratios of convex height to fiber diameter h/R_0 (g) and different angles θ between convex defect and contact point (h). (i) Simulated transferred charges of the dielectric fiber with different number of convex defects. The inset is a schematic diagram of the dielectric fiber with multiple convex defects.

Please cite this article in press as: R. Cheng et al., Materials Today (2025), https://doi.org/10.1016/j.mattod.2025.01.013

obtained through simulation and experiment has good consistency. In addition, both simulation and experimental results indicate that all microstructures have a positive impact on CE under high external forces ($\geq$0.1 N mm^{-1} in simulation and $\geq$0.25 N mm^{-1} in the experiment). Similar results can be found in triboelectric fiber with micro-scale concave defects (Fig. S20). Taking the convex defect as an example, it can be found that there are more non-contact regions around the convex under small external force, which is not conducive to charge transfer (Fig. 4d and e). However, the effective contact areas of the four microstructural defects increase compared to those without defects under high external forces, which will facilitate charge transfer (Fig. S19c). Therefore, the microstructure defect is favorable for CE under large external forces.

In order to observe and compare the distribution of local stress or charge density at defect locations, the charge density with and without defects was compared. For example, dielectric fiber with the convex defect has higher stress and charge density compared to that without defects, due to the accumulation of charges (Fig. 4c) caused by stress concentration at the defect location (Fig. S21). The simulated stress distribution nephogram and charge density distribution of the contact interface between the dielectric fiber with convex structure and conductive fiber under progressive loading are shown in Fig. 4d and e, respectively. In addition, the actual cross sectional view of the contact interface under different stress states are dispayed (Fig. 4f). Note that the stresses in Fig. 4f are not equal to the stresses in Fig. 4d and e. It can be found that the distribution trends of contact stress and charge density are consistent, and both increase with the increase of load. Due to the effect of convex microstructures, there are stress concentration zones and stress blind zones simultaneously under different loads, which determines the uneven distribution of surface charges. As for the full range of stress and charge density curves, Fig. S22 show the stress and charge density distribution of a convex (diameter is 10 μm) on the surface of a 3 mm diameter fiber under a force of 0.05 N mm^{-1}. It can be found that the curved surface of the fibers results in a parabolic uneven distribution of stress and charge density (Fig. S22a and c). Moreover, on the one hand, the convex will result in a greater stress and charge density (Fig. S22b and d). On the other hand, convex can also cause non-contact area, which is not conducive to charge transfer (Fig. S22b and d). In addition to the convex, three other microstructural defects have also been investigated (Fig. S23–S26). For the concave, the contact region extends from two edges towards the center of the concave, thereby determining the distribution of stress and charge density (Fig. S23). The stress concentration point and charge enrichment region are located at the concave boundary. The stress and charge density distribution of crack defects are similar to those of concave, except that crack defects are smaller and longer, requiring a larger load for stress extension (Fig. S24). The comparison of two types of invaginated defects, concave and crack, as well as their differences in CE behaviors, are analyzed in detail in Fig. S25 and Note S7. As an irregular extensional defect, the hairiness is always located in the area of stress concentration and charge density enrichment (Fig. S26).

Contact intensity is an important qualitative parameter in CE, which is positively correlated with the contact stress and contact area. The contact intensity (*CI*) is quantified by the integral of contact stress, and can be calculated as $CI = \int P(x)dx$, where $P(x)$ is the stress at position x. The influence of several structural parameters of convex microstructure defects on CE behaviors was simulated and analyzed in detail, including the ratio of convex height to fiber diameter (h/R_0), the angle between convex defect and contact point (θ), and the number of convex defects. It can be found that charge relative increment decreases with the increase of the h/R_0 (Fig. 4g). As the h/R_0 increases under the same stress conditions, the percentage of contacted area and the relative increment of contact intensity decrease, resulting in a decrease in the charge relative increment (Fig. S27). In addition, the charge relative increment decreases with the increase of the θ between the convex defect and the contact point (Fig. 4h), mainly due to the decrease in relative increment of contact intensity and the percentage of contacted area (Fig. S28) caused by the increase of the θ. Furthermore, the transferred charge shows a trend of first increasing then reaching saturation and final decreasing with the increase of the number of convex defects (Fig. 4i). The convex defects near the contact point facilitate charge transfer. However, the convex defects far from the contact point have smaller effective contact areas, resulting in lower stress and charge density (Fig. S29). Therefore, there exists an optimal distribution of the number of convex defects. In order to investigate the effect of defects on non-contact conditions, we simulated the potential distribution of the non-contact triboelectric fibers with and without convex defect. It is found that the convex will enhance the space potential (Fig. S30). Therefore, for both contact and non-contact states, the convex has a beneficial effect on contact electrification.

Influence of overall macrostructural compositions on CE

As previously introduced, the overall macrostructural compositions of triboelectric fibers mainly include different encapsulation processes of surface dielectric layers and different arrangement methods of conductive layer and dielectric layer. Although triboelectric fibers with different macrostructures have been designed to adapt to corresponding application scenarios, there is still a lack of systematic summary and detailed discussion (Table S5). Uniform coating and spiral coiling are the most widely used encapsulation methods of dielectric layers for triboelectric fibers, which can be accurately constructed with the same dielectric layer thickness by the molding or 3D printing method. The detailed modeling standards are shown in Fig. S31 and further discussed in Note S8. The measured transferred charges of the two encapsulation methods under the progressive loading are shown and compared in Fig. 5a. The transferred charges of coating method are larger than those of coiling method. To analyze the potential reason, the effective contact area between the dielectric fibers prepared by the two encapsulation methods and conductive fibers is simulated and calculated (Fig. 5b). It can be found that the coating method has a larger effective contact area when in contact with the same load, which is more conducive to increasing the amount of interfacial charge transfer. The stress distributions of the two encapsulation methods in contact state are also simulated and observed. As shown in Fig. 5c and d, the stress distribution of the coiling and coating combination structure shows a trend of center diffusion at the contact point and

Please cite this article in press as: R. Cheng et al., Materials Today (2025), https://doi.org/10.1016/j.mattod.2025.01.013

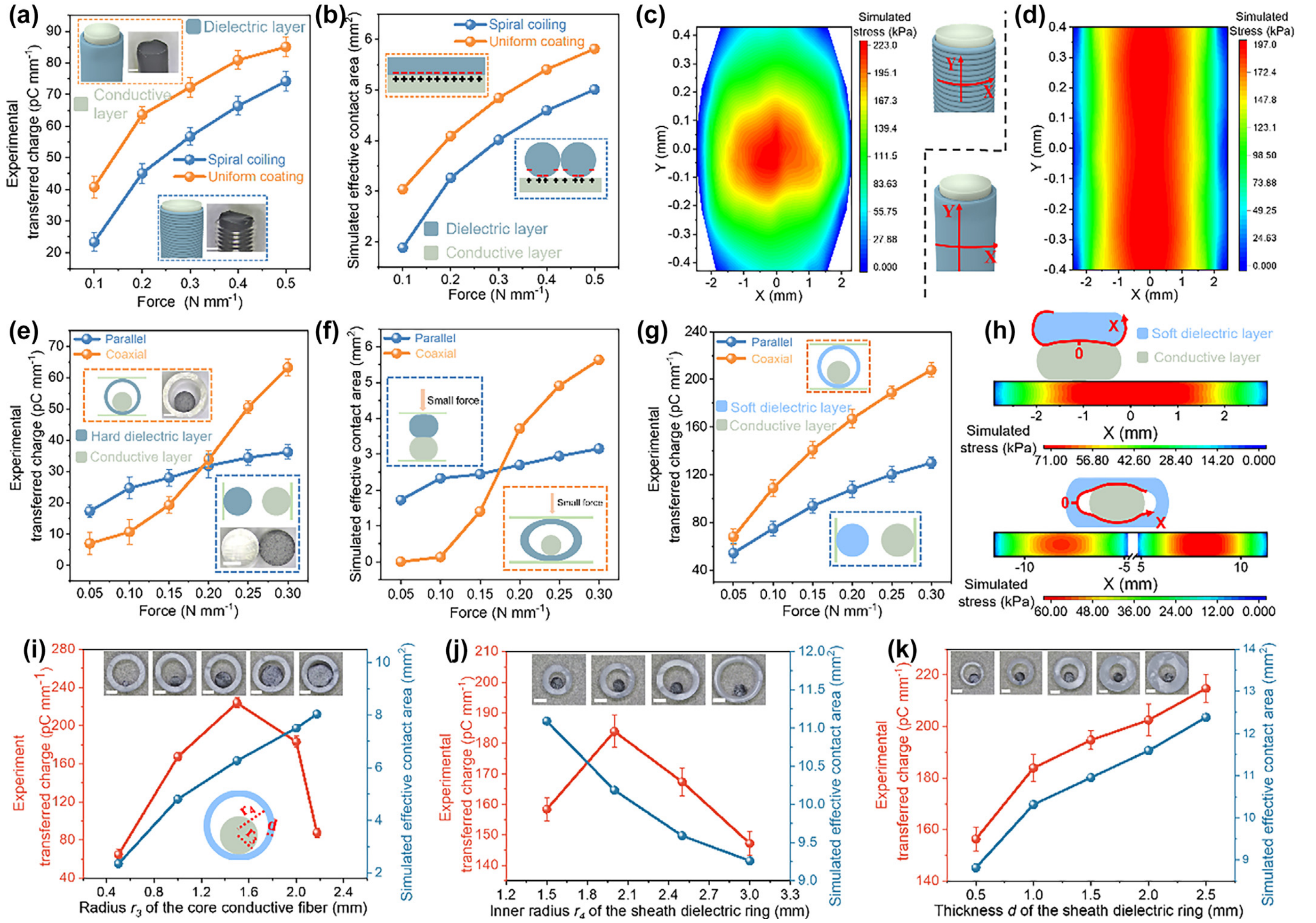

FIG. 5

Influence of overall macrostructural compositions on CE behaviors. (a and b) Comparison of experimental transferred charges (a) and simulated effective contact area (b) between spiral coiled dielectric layer and uniform coated dielectric layer under progressive loading. The inset in (a) is the physical images and schematic diagrams of two types of triboelectric fibers. The inset in (b) is the schematic diagrams of the cross-sectional charge distribution of triboelectric fibers with spiral coiled and uniform coated dielectric layers. Scale bar is 2 mm. (c and d) Simulated stress distribution nephogram of spiral coiled (c) and uniform coated (d) triboelectric fibers in contact state. The insets are the schematic diagrams of the coordinate system. (e-f) Comparison of core-sheath coaxial and parallel arrangement triboelectric fibers in experimental transferred charges (e) and simulated effective contact area (f). (e, g) Comparison of core-sheath coaxial and parallel arrangement triboelectric fibers with high modulus (e) and low modulus (g) dielectric layer in experimental transferred charges. The insets in (e) are the schematic diagrams and physical photographs of the coaxial and parallel arrangement triboelectric fibers. The insets in (f) are the schematic diagram of the deformation of coaxial and parallel triboelectric fibers prepared by high modulus dielectric layers. Scale bar is 2 mm. (h) Comparison of contact status and stress distributions of the coaxial and parallel structured triboelectric fibers. (i–k) Experimental transferred charge and simulated effective contact area of the coaxial triboelectric fibers under different structural parameters, including the radius of the core conductive fiber r_3 (i), the inner radius of the sheath dielectric ring r_4 (j), and the thickness of the sheath dielectric ring d (k). The cross-sectional photographs of coaxial triboelectric fibers with different structural parameters are shown above in (i–k). The detailed schematic diagram of structural parameters is shown below in (i). Scale bar is 2 mm.

uniform distribution at the contact surface, respectively. The coordinate systems of the coiling and coating structure are also inserted in Fig. 5c and d, respectively. The spiral coiling method exacerbates the uneven contact between the dielectric fiber and the conductive fiber, resulting in a smaller effective contact area and less transferred charge than the coating structure. In addition, the influence of the radius of the spiral coiling dielectric fibers (r_1) and the radius of the inner core fiber electrode (r_2) on the CE behaviors of the coiling structure is further explored. It is found that both the transferred charge and effective contact area present a trend of first increasing and then decreasing with the increase of r_1 (Fig. S32). A larger inner fiber radius r_2 is more conducive to effective contact with its surface coiled dielectric fibers, thus improving the interfacial charge transfer (Fig. S33).

In addition to the encapsulation method of dielectric layer, the arrangement mode between dielectric fibers and conductive fibers is also important, mainly including the coaxial core-sheath structure and the axial parallel structure. Due to the significant correlation between the CE behaviors of triboelectric fibers and the deformation ability of dielectric layers (i.e. modulus), the influence of dielectric layers with different moduli on CE has also been analyzed. The fitted strain–stress curve and stress-charge density curve of the high-modulus dielectric layer are shown in Fig. S34. For the dielectric layer with high modulus,

Please cite this article in press as: R. Cheng et al., Materials Today (2025), https://doi.org/10.1016/j.mattod.2025.01.013

the experimentally measured transfer charge density and simulated effective contact area are shown in Fig. 5e and f, respectively. Under low stress conditions, high modulus dielectric layers have better resistance to deformation, resulting in smaller effective contact area and transferred charge of the coaxial mode compared to the parallel mode. However, under high stress conditions, the deformation of the high modulus dielectric layer becomes more pronounced, resulting in a larger effective contact area between the dielectric layer and the conductive layer of the coaxial structural fiber, thus having more transferred charge. When the encapsulation dielectric layer has a low modulus, the effective contact area and interfacial charge transfer of the coaxial structure are higher than those of the parallel structure under different loads (Figs. 5g and S35). Similar results are found in two-electrode mode triboelectric fibers (Fig. S36). In order to further compare the differences in CE behavior between the coaxial structural and parallel structural triboelectric fibers, the cross-sectional stress distribution of the two combination structures is compared (Fig. 5h). The effective contact area of coaxial triboelectric fibers is much higher than that of parallel structures, resulting in more interfacial charge transfer.

Due to the better electrical output performance of coaxial triboelectric fibers, their basic structural parameters have been further investigated in detail, including the radius of the core conductive fiber (r_3), the inner radius of the sheath dielectric ring (r_4), and the thickness of the sheath dielectric ring (d). It should be noted that coaxial triboelectric fibers with different structural parameters are also accurately prepared through molding or 3D printing methods. It can be found that as the r_3 increases, the effective contact area between the conductive layer and the dielectric layer gradually increases, while the interfacial transferred charge shows a trend of first increasing and then decreasing (Fig. 5i). When r_4 remains constant, the increase in r_3 will narrow the gap between the core conductive layer and the sheath dielectric layer, thereby weakening the electrostatic induction effect and further reducing the transferred charge. As a result, there exists an optimal r_3 under the trade-off effect between increased effective contact area and weakened electrostatic induction. The relative contact area and transferred charge of coaxial triboelectric fibers are quantitatively analyzed under different inner radii of the sheath dielectric ring r_4. As shown in Fig. 5j, as the r_4 increases, the relative contact area gradually decreases, and transferred charge shows a characteristic of first increasing and then decreasing, which is also caused by the increase in contact area and the weakening of electrostatic induction. Therefore, there also exists an optimal r_4. When the gap distance between the conductive layer and the dielectric layer remains constant, that is r_3 and r_4 are constant, an increase in the thickness of the dielectric layer d increases the effective contact area and charge transfer (Fig. 5k), indicating that the thickness of the dielectric layer has a positive effect on increasing charge transfer within a certain range. The comparison of different macrostructural compositions is also summarized in Table S6. By studying the overall macrostructural composition of triboelectric fibers, we not only understand the influence laws of different encapsulation and combination methods on CE behaviors, but also grasp the detailed parameter design scheme of coaxial and uniform coating triboelectric fibers, providing theoretical guidance for designing high-performance triboelectric fibers.

Discussion

In summary, the influence laws and potential mechanisms of surface microstructural defects and overall macrostructural compositions of triboelectric fibers on their CE behaviors have been explored in detail through a combination of precise experimental measurements and finite element simulations. Based on the positive correlation between stress and charge, a novel surface charge density distribution characterization method for micrometer scale is proposed, which can accurately and quantitatively observe the charge distribution at the microstructure of triboelectric fibers. The difference of CE behaviors between curved fiber structure and planar film structure indicates that the stress and charge density of fiber–fiber are higher than that of film-film. The large charge dissipation mainly exists in the charge enrichment area at the fiber contact point and in the contact state with the conductor. Different surface microstructural defects act as stress concentration regions during the contact process, leading to local accumulation of induced charges, which is beneficial for improving the overall transferred charges. The influence of convex structural parameters on CE behavior has also been discussed in detail. For the encapsulation method of dielectric layer, the coating structure has a more uniform stress distribution and more effective contact area than the spiral coiling structure, thus having a higher transferred charge. The coaxial core-sheath structure has a larger effective contact area under high stress conditions compared to the parallel arrangement structure, thus having higher charge transfer capacity. The basic structural parameters of the coaxial triboelectric fibers are also quantitatively measured and analyzed.

This work focuses on the special structural characteristics of a new type of wearable energy harvesting smart textiles, i.e. triboelectric fibers, proposes a quantitative characterization method for the surface charge density distribution of microstructures, and clarifies the influence law and mechanism of macro and micro structures on CE, which not only provides a new research paradigm for exploring the CE behaviors of complex structures, but also lays a theoretical foundation for designing high-performance triboelectric fibers from the perspective of structural optimization.

Methods

Preparation of the dielectric fibers

In this work, all triboelectric fibers were prepared by template injection molding or 3D printing method. Dielectric elastomers, ecoflex 0030 (~0.62 kPa, Smooth-on) and PDMS (~1.1 MPa, Dowcorning 184) were adopted as the low and high modulus dielectric layers, respectively. Particularly, ecoflex solution was prepared by mixing two components with the mass ratio of 1:1. And PDMS solution was prepared by mixing the basic components and curing agent with the mass ratio of 10:1. For the dielectric layers without surface microstructural defects, the polytetrafluoroethylene (PTFE) hollow tube with smooth inner wall was selected as the mold, due to the excellent detachment of ecoflex and PDMS. The precursor solutions of ecoflex and PDMS

Please cite this article in press as: R. Cheng et al., Materials Today (2025), https://doi.org/10.1016/j.mattod.2025.01.013

were injected into PTFE tubes of different diameters by the syringe pump, and cured in an oven at 100 °C for 1 h. Among them, the inner diameter of the finest PTFE hollow tube was 0.3 mm. An ultrafine needle was used to squeeze the precursor solution into finer PTFE hollow tubes. In addition, more precise 3D printing methods made of RC30 red wax with an accuracy of 50 μm was chosen for the dielectric layers with the surface microstructural defects. The precursor solution was poured into the 3D printing model and then cured in the oven.

Preparation of the conductive fibers

2.5 wt% carbon micron/nanofibers suspension provided by XFNANO company was filled into the ecoflex 0030 precursor solution to prepare the conductive mixed solution. Subsequently, the mixed solution was stirred well and injected into the PTFE hollow tube or 3D printed mold. Finally, the conductive fibers with variable diameters could be obtained after curing in a 100 °C oven for 1 h.

Preparation of different dielectric layers for the coaxial triboelectric fibers

In order to accurately control the thickness and diameter of the outer dielectric sheath layers of the coaxial triboelectric fiber, two hollow steel pipes are sleeved together as the mold. The outer diameter of the inner steel tube was the inner diameter of the sheath layer, while the inner diameter of the outer steel tube was the outer diameter of the sheath layer. These two steel pipes were coaxially inserted into a 3D printed mold. Subsequently, the precursor solution was perfused between the two steel pipes to form the outer sheath layer. Here, rigid steel pipes were chosen instead of PTFE pipes to maintain parallel arrangement along the length direction.

Preparation of the dielectric films and the conductive films

The dielectric films and the conductive films were prepared by ecoflex solution and conductive ecoflex solution, respectively. The precursor solution was poured into a PTFE mold and placed in a 100 °C oven for 1 h. As for the film-film contact pairs, the length and width of the films were equal to the circumference of the fibers, and the thickness of the films was 0.5 mm. Finally, the films were attached to acrylic plates using 3 M tapes for further electrical performance measurement.

Finite element simulation

Commercial finite element simulation software ANSYS Workbench (version 2021, R2) was adopted for stress distribution analysis. In this study, in order to simplify the simulation, the dielectric layer and conductive layer are assumed to be incompressible materials. Their mechanical properties were captured by three-parameter Mooney-Rivlin strain potential constitutive model. The strain energy density is $W = C_{10}(\bar{I}_1 - 3) + C_{01}(\bar{I}_2 - 3) + C_{11}(\bar{I}_1 - 3)(\bar{I}_2 - 3)$, where $\bar{I}_1$ and $\bar{I}_2$ were the first and second invariants of the left Cauchy-Green deformation tensor, respectively. C_{10}, C_{01} and C_{11} were the material parameters, which could be obtained by fitting the stress–strain curves and then imported into the material data in ANSYS Workbench. As for the models, two baffles with material properties of the structural steel were placed on either side of the models to apply a uniform external force. The contacts between fiber models and between fiber models and baffles were set as frictional contact. A fine mesh was constructed (unit size of microstructure defects < 2×10^{-6} m) to ensure computational accuracy. The initial, minimum and maximum substeps were selected as 5000, 2000 and 50000, respectively. As for the model types, the comparison between uniform coating and spiral coiling was simulated using 3D models, while others were simulated with 2D models. As for the size of the model, the diameter of the dielectric fibers with microstructures was 3 mm, the width of the film was 3π mm (fiber-film) or 3 mm (film-film), and the thicknesses of the thin film and the thick film were 0.1 mm or 3 mm, respectively.

Measurement of surface potential distribution

There are two difficulties in measuring the surface potential distribution of dielectric fibers using an electrostatic voltmeter. Firstly, it was difficult for the probe with the size of $10 \times 10\ mm^2$ to accurately measure the surface potential of the fibers with diameters below 10 mm. Secondly, it was also difficult to measure the surface potential distribution of dielectric fibers by moving the probe through traditional 2D platforms. In order to verify the accuracy of the novel microscale charge density distribution characterization method, it was necessary to measure and compare the surface potential distribution of dielectric fibers with electrostatic voltameters. Several coarse dielectric fibers with the diameter of 20 mm were prepared. The distance between the probe and the surface of the dielectric fiber should be kept consistent. Two low-speed rotating motors were used to keep the dielectric fibers rotating at a constant speed. The probe was fixed at a position 1 mm above the surface of the dielectric fiber. Therefore, during the rotation of the dielectric fiber, the distance between the probe and the surface of the polymer fiber could be kept constant. Finally, the surface potential distribution of triboelectric fibers could be measured.

Characterizations

The surface morphology and microstructural defects of triboelectric fibers were characterized by field emission scanning electron microscope (Nova 450, FEI). The relative movement of triboelectric fibers or films was driven by a linear motor (LinMot E1200) for electrical output performance measurements. The software platform was constructed on the basis of LabVIEW. The loading force was accurately measured or quantitatively controlled by a dynamometer (DFS-BTA). The transferred charge density was measured by a programmable electrometer (Keithley, model 6514). The precursor solution was injected into the mold through a syringe pump (LSP01-2A). The surface potential was tested by an electrostatic voltmeter (Trek 341B). The mechanical properties of the elastomer are tested by Instron E3000. The functional groups are characterized by Fourier Transform Infrared Spectroscopy (Vertex 80v).

CRediT authorship contribution statement

Renwei Cheng: Writing – original draft, Visualization, Validation, Methodology, Investigation, Data curation, Conceptualization. **Chuanhui Wei:** Validation, Methodology, Formal analysis, Data curation. **Chuan Ning:** Validation, Supervision,

Please cite this article in press as: R. Cheng et al., Materials Today (2025), https://doi.org/10.1016/j.mattod.2025.01.013

Methodology, Formal analysis, Data curation. **Tianmei Lv:** Visualization, Validation, Supervision, Formal analysis, Data curation. **Xiao Peng:** Supervision, Software, Resources, Methodology, Investigation, Formal analysis, Data curation. **Zhong Lin Wang:** Writing – review & editing, Visualization, Supervision, Software, Resources, Project administration, Investigation, Funding acquisition. **Kai Dong:** Writing – review & editing, Writing – original draft, Supervision, Software, Resources, Project administration, Methodology, Investigation, Funding acquisition, Formal analysis, Data curation, Conceptualization.

Data availability

Data will be made available on request.

Declaration of competing interest

The authors declare that they have no known competing financial interests or personal relationships that could have appeared to influence the work reported in this paper.

Acknowledgements

The authors are grateful for the support received from the National Natural Science Foundation of China (Grant No. 22109012), Natural Science Foundation of the Beijing Municipality (Grant Nos. L222037 and 2212052), the Postdoctoral Fellowship Program of CPSF (Grant Nos. GZB20240297 and GZB20230328), China Postdoctoral Science Foundation (Grant No. 2024M751716), Science Technology and Innovation Committee of Shenzhen Municipality (Grant No. JCYJ20240813094924033), the National Key R & D Project from the Ministry of Science and Technology (Grant No. 2021YFA1201601), the Fundamental Research Funds for the Central Universities (Grant No. E1E46805), and the ShuiMu Tsinghua Scholar Program.

Appendix A. Supplementary material

Supplementary material to this article can be found online at https://doi.org/10.1016/j.mattod.2025.01.013.

References

[1] E. Fukada, J.F. Fowler, *Nautre* 181 (1958) 693.
[2] R.G. Horn et al., *Nature* 366 (1993) 442.
[3] W. Xu et al., *Nature* 578 (2020) 392.
[4] P.E. Shaw, *Nature* 118 (1926) 659.
[5] Z.L. Wang, A.C. Wang, *Mater. Today* 30 (2019) 34.
[6] Z. Wang et al., *Chem. Soc. Rev.* 53 (2024) 4349.
[7] F. Liang et al., *Nano Energy* 69 (2020) 104414.
[8] F. Liang et al., *Adv. Energy Mater.* 12 (2022) 2102991.
[9] Q. Sun et al., *Adv. Mater.* 35 (2023) 2210915.
[10] Q. Sun et al., *Adv. Mater.* 36 (2024) 2307918.
[11] H. Guo et al., Sci. Rob. 3 (2018) eaat2516.
[12] S.R. Barman et al., Sci. Adv. 9 (2023) eadc8758.
[13] S.R. Barman et al., *ACS Nano* 17 (2023) 2689.
[14] A. Li et al., *Nat. Nanotechnol.* 12 (2017) 481.
[15] H. Guo et al., *Nat. Sustain.* 4 (2020) 147.
[16] J. Shen et al., *Biosens. Bioelectron.* 216 (2022) 114595.
[17] S. Lin et al., *Nat. Commun.* 13 (1) (2022) 5230.
[18] D. Choi et al., *ACS Nano* 17 (2023) 11087.
[19] C. Dong et al., *Nat. Commun.* 11 (2020) 3537.
[20] A. Khan et al., *Nano Energy* 119 (2024) 109051.
[21] S. Li et al., *Adv. Mater.* 32 (2020) 2001307.
[22] D. Liu et al., *Nat. Commun.* 13 (2022) 6019.
[23] K. Dong et al., *Adv. Mater.* 32 (2019) 1902549.
[24] L. Wu et al., *Mater. Horiz.* 11 (2024) 341.
[25] C. Lu et al., *Nature* 629 (2024) 86.
[26] C. Chen et al., *Chem. Rev.* 123 (2) (2022) 613.
[27] A. Linarts et al., *Small* 19 (2023) 2205563.
[28] A. Šutka et al., *Adv. Energy Sustainability Res.* 5 (2024) 2300259.
[29] K. Dong et al., *Adv. Mater.* 34 (2022) 2109355.
[30] J. Jeong et al., *Polymers* 11 (2019) 1443.
[31] K. Fu et al., *Nano Energy* 88 (2021) 106258.
[32] M. Chen et al., *Nat. Commun.* 12 (2021) 1416.
[33] C. Wei et al., *Adv. Funct. Mater.* (2023) 2303562.
[34] F. Zhan et al., *ACS Nano* 14 (2020) 17565.
[35] S. Lin, Z.L. Wang, *Appl. Phys. Lett.* 118 (2021) 193901.
[36] H. Zou et al., *Nat. Commun.* 10 (2019) 1427.
[37] H. Zou et al., *Nat. Commun.* 11 (2020) 2093.
[38] J. Zhang et al., *ACS Nano* 15 (9) (2021) 14830.
[39] H. Qin et al., *Adv. Funct. Mater.* 32 (2022) 2111662.
[40] Z. Tang et al., *J. Phys. Chem. C* 126 (2022) 8897.
[41] A. Šutka et al., *Adv. Mater. Technol.* 7 (2022) 2200162.
[42] O. Verners et al., *Nano Energy* 104 (2022) 107914.
[43] R. Cheng et al., *ACS Nano* 14 (2020) 15853.
[44] H. Kou et al., *ACS Appl. Mater. Interfaces* 14 (2022) 23998.
[45] Y. Lu et al., *Nat. Commun.* 13 (2022) 1401.
[46] Z.L. Wang, *Rep. Prog. Phys.* 84 (2021) 096502.
[47] F. Sheng et al., *ACS Appl. Mater. Interfaces* 13 (2021) 44868.
[48] X. Yu et al., *Energy Convers. Manag.* (2022) 263.
[49] M. Zhang et al., *Matter* 1 (2019) 168.
[50] M.M. Hasan et al., *Small* 19 (2022) 2206107.
[51] Y. Li et al., *Adv. Fiber Mater.* 4 (2022) 1584.
[52] K.Y. Lee et al., *Adv. Mater.* 26 (2014) 5037.
[53] R. Wen et al., *Adv. Funct. Mater.* 29 (2019) 1807655.
[54] F. Galembeck et al., *Chem. Soc. Rev.* 53 (2024) 2578.

Please cite this article in press as: R. Cheng et al., Materials Today (2025), https://doi.org/10.1016/j.mattod.2025.01.013